Springer

KSME

Journal of Mechanical Science and Technology 31 (5) (2017) 2261~2277
www.springerlink.com/content/1738-494x(Print)/1976-3824(Online)
DOI 10.1007/s12206-017-0423-7

Leakage and rotordynamic performance of a mixed labyrinth seal compared with that of a staggered labyrinth seal [†]

Mingjie Zhang, Jiangang Yang*, Wanjun Xu and Yalei Xia
National Engineering Research Center of Turbo-generator Vibration, Southeast University, Nanjing, China

(Manuscript Received May 4, 2016; Revised December 29, 2016; Accepted January 18, 2017)

Abstract

Minimizing unwanted leakage between stationary and rotating parts is the main function of annular seals. A Mixed labyrinth seal (MLS) with two specially designed lateral teeth installed on a Staggered labyrinth seal (SLS) is proposed to improve seal performance. A 3D computational fluid dynamics calculation model of MLS is set up. The twin vortex structure that appears in the seal cavity and flow path is more complicated in MLS than in SLS. MLS reduces leakage by about 30 % compared with SLS. Rotordynamic analysis of MLS is also conducted by calculating cross-coupled stiffness. The cross-coupled stiffness of MLS is about 75 % to 85 % that of SLS. The dependence of seal performance on the parameters of the lateral teeth is investigated through a simulation test. The lateral teeth should be set in the middle of the seal cavity, and the gap between the two lateral teeth should be similar to the tip clearance.

Keywords: Seal; Lateral teeth; Leakage; Rotordynamic performance; Computational fluid dynamics

1. Introduction

Annular seals represent an important flow element in gas and steam turbines. Minimizing unwanted leakage between stationary and rotating parts is the main function of annular seals. Leakage reduction is essential for improving the performance of current and advanced turbines. For example, reducing the seal leakage of gas-produced air by 1 % in an advanced transport engine yields a 1 % increase in engine thrust and a 0.1 % decrease in Specific fuel consumption (SFC) [1]. For an advanced fighter engine, a 1 % reduction in high-pressure turbine seal leakage results in a 0.3 % decrease in SFC and a 0.8 % increase in thrust [1].

Labyrinth seals are widely used in turbines and compressors despite the recent development of several advanced sealing techniques. Labyrinth seals are characterized by a high pressure ratio, simple structure, and high reliability. With the improvement of turbines, the clearances of labyrinth seals have become more tightly designed and controlled than before to reduce seal leakage and improve turbine efficiency. However, seal clearance should be maintained above a certain minimum value to avoid rubbing between the stator and rotor. Modern industrialization of practical turbomachinery systems necessitates the use of complex high-performance labyrinth seals with a special arrangement of knife teeth or structures to reduce seal leakage further without a considerable reduction in annular clearance. For example, the simplest straight-through labyrinth seal was developed to the stepped and Staggered labyrinth seals (SLS) (Fig. 1).

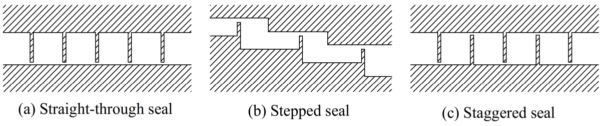
(a) Straight-through seal (b) Stepped seal (c) Staggered seal

Fig. 1. Three types of labyrinth seals.

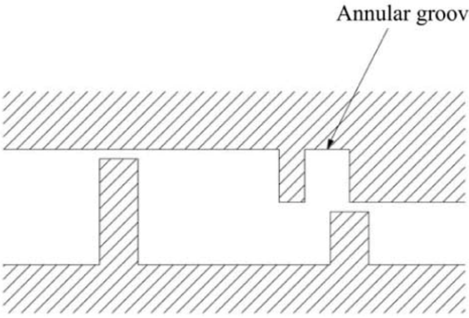

Fig. 2. Stepped seal with an annular groove.

Modern eye seals are often designed as stepped seals, and the balance drum seal usually employs SLS in a typical centrifugal compressor [2, 3]. Compared with the straight-through labyrinth seal, the two other types of labyrinth seals are constructed with an axially serpentine flow path, and the sudden

---

*Corresponding author. Tel.: +86 13951988554, Fax.: +86 2583794684
E-mail address: jgyang@seu.edu.cn

† Recommended by Associate Editor Sangyoup Lee

© KSME & Springer 2017

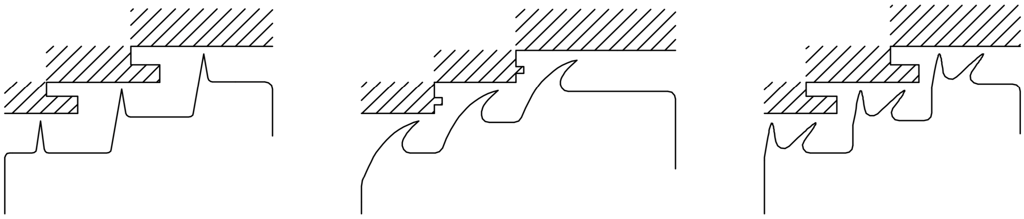

(a) Step with land turbulence generator

(b) Slanted step with land turbulence generator

(c) Paired knives

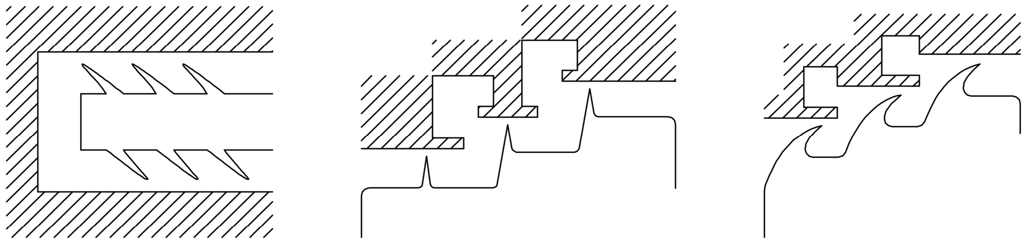

(d) Back-to-back slanted knife seal

(e) Step seal with swirl cavity trap

(f) Slanted step seal with swirl cavity

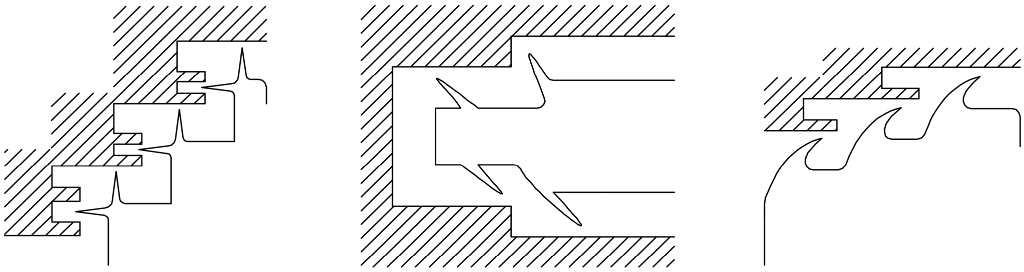

(g) Radial step seal with axial spoiler

(h) Back-to-back slanted step seal

(i) Slanted step seal with trapped swirl ejection

Fig. 3. Sketches of seal configurations.

deflection of the main fluid is related to leakage resistance [4, 5]. With a similar design concept, an advanced labyrinth seal that possesses an annular groove was proposed to increase leakage resistance (Fig. 2). Rhode et al. [5] utilized a water leakage and flow visualization test facility to study leakage resistance and observed an increase of 26 % over the baseline design. Stocker [1] proposed nine unique labyrinth seal configurations by increasing the number of seal knives and knife pitch and employing unique geometries, as shown in Fig. 3. In three test and evaluation phases, the final labyrinth seal designs showed improvements of 10 % to 25 % in leakage loss. All of these studies showed that the labyrinth seal structure is becoming increasingly complex and that effective labyrinth seal geometries should provide a highly frictional flow path [6] and exhibit increased internal cavity turbulence [1, 7]. Studies on the seal structure and its effect on leakage reduction are still underway.

Although the primary function of annular seals is to prevent leakage, labyrinth seals possess certain undesirable rotordynamic characteristics that are mainly related to instability. Circumferential flow induces the destabilizing force represented by cross-coupled stiffness [8], which is the primary cause of instabilities originating from labyrinth seals [9]. Given that preswirl velocity at the labyrinth seal entrance exerts a significant influence on cross-coupled stiffness [10, 11], swirl brakes [12] and "negative-swirl" brakes [13] are employed to brake or reverse the circumferential direction of inlet flow. Investigations have shown that the swirl brake reduces destabilizing cross-coupled stiffness k by a factor of 0.8, and the negative-swirl brake changes the sign of k at an appreciable magnitude [13]. In addition, labyrinth seals offer only limited damping of rotor vibration; as a result, the bearing locations are the only feasible locations to add significant damping. Thus, damper seals, such as pocket damper and honeycomb seals (shown in Fig. 4), with large amounts of damping have a great potential to suppress rotor vibration effectively. Vance et al. [8] showed that the pocket damper seal (TAMSEAL) exhibits positive effective damping; while, the effective damping of the conventional seal is not only small but also negative for inlet air pressure exceeding 2 bar (30 psia). Soto et al. [14] showed that the honeycomb seal provides larger effective damping than the labyrinth seal with-

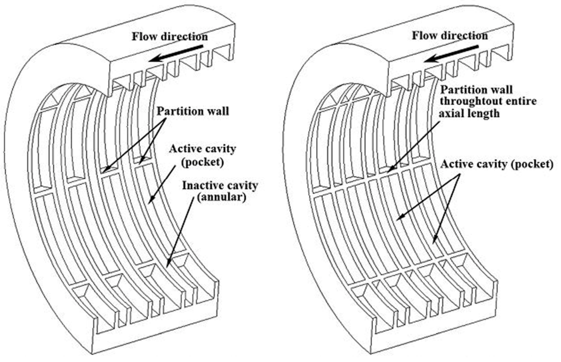

(a) Pocket damper seal (Li et al. [16])

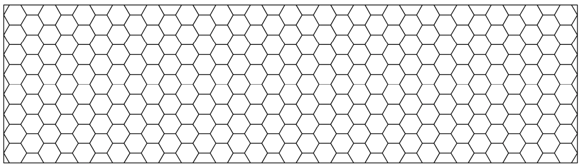

(b) Honeycomb seal

Fig. 4. Damper seals.

out injection, and the magnitude of effective damping is insensitive to running speed and increases with the increase in the pressure ratio. However, the leakage characteristics of the honeycomb seal are not always better than those of the labyrinth seal [15]. Seal leakage and rotordynamic performance should be considered simultaneously.

A Mixed labyrinth seal (MLS) was proposed in this study to improve the comprehensive performance of the seal by adding lateral teeth to SLS. A 3D Computational fluid dynamics (CFD) method was established to analyze the leakage and rotordynamic performance of this seal. Comparisons were conducted between MLS and SLS.

2. MLS with lateral teeth

This study assumed that enhancing throttling and turbulence in the seal cavity is important for leakage control. MLS was presented on the basis of SLS, with two specially designed lateral teeth installed on the vertical teeth of SLS (Fig. 5).

Leakage depends on a number of parameters, such as the number of cavities, tip clearance, and pressure ratio. The flow through the labyrinth seal can be considered a series of throttling processes. According to the Kearton–Keh equation [17], the mass flow rate through a throttle can be described as

$$\frac{M}{A} = \sqrt{\frac{\beta(P_0^2 - P_n^2)}{R_g T_0}}\ , \tag{1}$$

where M is the mass flow rate, A is the flow area, P_0 is the inlet pressure, P_n is the outlet pressure, T_0 is the inlet total temperature, R_g is the gas constant, and β is a function of P_0 / P_n.

This study also assumed that the pressure ratio of the last throttle is less than the critical pressure ratio and that the β coefficients at each throttle are similar.

For SLS, as shown in Fig. 5(a), the mass flow rate equation passing each seal tip has the same form, namely,

$$\begin{aligned}
P_0^2 - P_1^2 &= \frac{R_g T_0}{\beta}\left(\frac{M_{SLS}}{A_1}\right)^2 \\
P_1^2 - P_2^2 &= \frac{R_g T_0}{\beta}\left(\frac{M_{SLS}}{A_2}\right)^2 \\
\vdots \qquad & \qquad \vdots \qquad\qquad , \\
P_{n-2}{}^2 - P_{n-1}{}^2 &= \frac{R_g T_0}{\beta}\left(\frac{M_{SLS}}{A_{n-1}}\right)^2 \\
P_{n-1}{}^2 - P_n^2 &= \frac{R_g T_0}{\beta}\left(\frac{M_{SLS}}{A_n}\right)^2
\end{aligned} \tag{2}$$

where M_{SLS} is the mass flow rate of SLS, P_i is the pressure in the ith seal cavity, n is the number of seal teeth, and A_i is the flow area of the ith orifice. The mass flow rate can be derived as

$$M_{SLS} = \sqrt{\frac{\beta(P_0^2 - P_n^2)}{R_g T_0 (\sum_{i=1}^{n} \frac{1}{A_i^2})_{SLS}}}\ . \tag{3}$$

For MLS, the mass flow rate equation passing each clearance can be described as

$$\begin{aligned}
P_0^2 - P_{1,1}{}^2 &= \frac{R_g T_0}{\beta}\left(\frac{M_{MLS}}{A_1}\right)^2 \\
P_{1,1}{}^2 - P_{1,2}{}^2 &= \frac{R_g T_0}{\beta}\left(\frac{M_{MLS}}{B_1}\right)^2 \\
\vdots \qquad & \qquad \vdots \qquad\qquad . \\
P_{n\text{-}1,1}{}^2 - P_{n\text{-}1,2}{}^2 &= \frac{R_g T_0}{\beta}\left(\frac{M_{MLS}}{B_{n\text{-}1}}\right)^2 \\
P_{n\text{-}1,2}{}^2 - P_n^2 &= \frac{R_g T_0}{\beta}\left(\frac{M_{MLS}}{A_n}\right)^2
\end{aligned} \tag{4}$$

The mass flow rate of MLS can be derived as

$$M_{MLS} = \sqrt{\frac{\beta(P_0^2 - P_n^2)}{R_g T_0 \left[(\sum_{i=1}^{n} \frac{1}{A_i^2})_{SLS} + (\sum_{i=1}^{n-1} \frac{1}{B_i^2}) \right]_{MLS}}}\ , \tag{5}$$

where B_i is the flow area of the ith lateral teeth gap.

Given that

$$(\sum_{i=1}^{n} \frac{1}{A_i^2})_{SLS} < \left[(\sum_{i=1}^{n} \frac{1}{A_i^2})_{SLS} + (\sum_{i=1}^{n-1} \frac{1}{B_i^2}) \right]_{MLS}\ , \tag{6}$$

the leakage of MLS is lower than that of SLS.

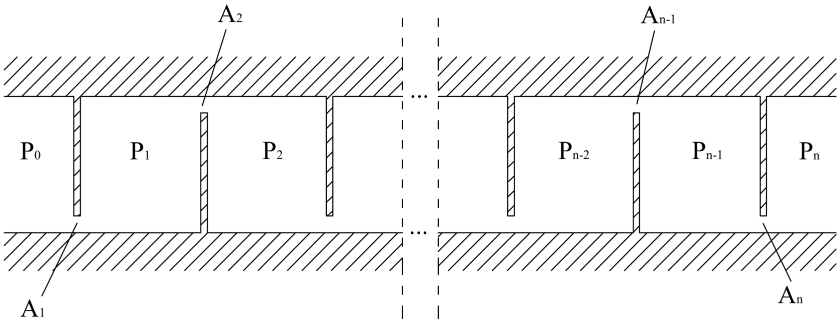

(a) SLS

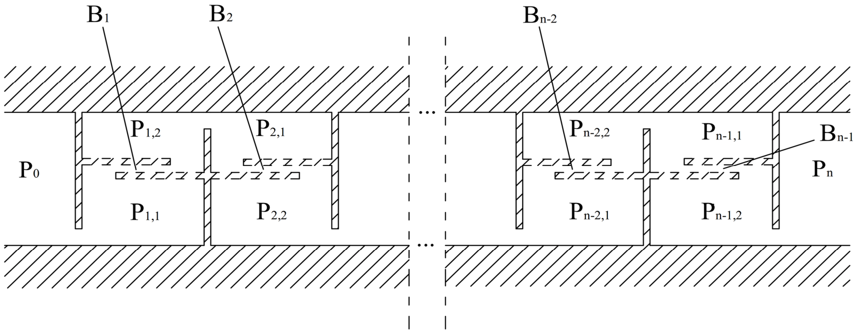

(b) MLS

Fig. 5. Schematic of SLS and MLS.

3. Numerical method

3.1 Solution techniques

Working fluid is assumed to be ideal gas. Given that the flow in the labyrinth seal exhibits 3D turbulence, the $k_t - \varepsilon_t$ two-equation turbulence model was employed to analyze the flow patterns in this study. k_t is the turbulence kinetic energy and is defined as the variance in the fluctuations in velocity. ε_t is the turbulence eddy dissipation.

This study did not use the $k_t - \omega_t$ model because it requires a strictly low Reynolds number and a near-wall grid resolution of at least $y+ < 2$; this condition cannot be guaranteed in most applications at all walls. The SST $k_t - \omega_t$ model is an improved model based on the $k_t - \omega_t$ model; it combines the advantages of $k_t - \omega_t$ and $k_t - \varepsilon_t$ models. The SST model has been partly used in seal simulation. However, the $k_t - \varepsilon_t$ model is still the most commonly used model to simulate the labyrinth seal because it can meet the requirements of excellent stability and good accuracy, and a large number of its numerical results exhibit good agreement with the experiment results [2, 3, 9, 11, 16, 22].

The commercial CFD code ANSYS FLUENT utilizes a pressure-based solver, which employs the finite-volume-based method to solve the equations for conservation of mass, momentum, and energy using the SIMPLE pressure–velocity coupling algorithm. Discretization schemes, such as least squares cell based for gradient; standard for pressure; second-order upwind for density, momentum, and energy; and first-order upwind for turbulent kinetic energy and dissipation rate, were selected in this study.

To obtain accurate wall shear stress, care was exerted to ensure that the near-wall grid points were placed in the logarithmic region. The model used utilizes the standard wall function, in which the value of $y+$ lies between 30 and 500.

3.2 Justification of the numerical method

The results were compared with that of the five-tooth seal example used by Hirano et al. [18] to verify the accuracy and reliability of the 3D CFD method. The same meshing scheme was used. The leakage of the CFD model and the result of Hirano et al. [18] are 1.15 and 1.08 kg/s, respectively. The relative error is 6.5 %. Fig. 6 shows a comparison of tangential force with that in previous work. The maximum error of tangential force was less than 15 %. A detailed introduction of numerical interpolation was not provided in Ref. [18], and the error may have originated from the difference in numerical interpolation. In addition, FLUENT software was used in this study, whereas CFX-TASCflow was used in Ref. [18]. Software error could not be avoided in the calculation.

Previous studies have used a linearized model to describe the force–displacement relationship [10, 18]. The relationship between tangential force and whirl speed is defined as

$$\frac{F_t}{\delta} = k - \Omega C , \tag{7}$$

where F_t is the tangential force, δ is the eccentricity, k is the

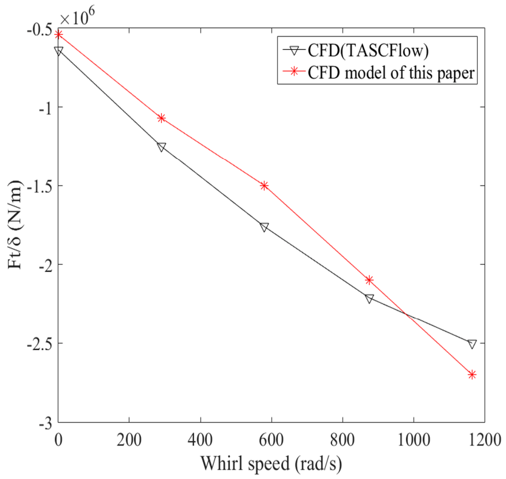

Fig. 6. Comparison of tangential force with that in previous work.

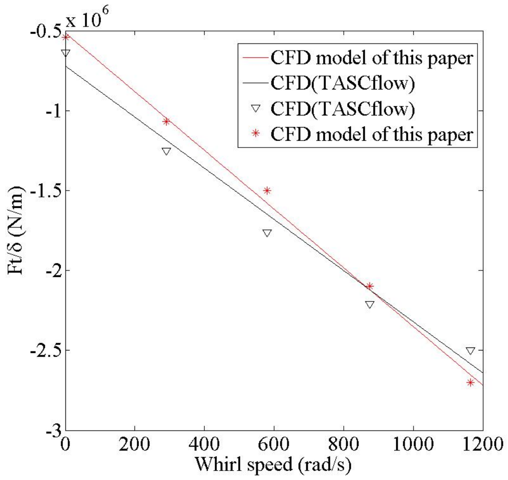

Fig. 7. Fitting curves of the two results.

cross-coupled stiffness, Ω is the whirl speed, and C is the direct damping.

According to the linearized model, the intercept on the y axis is cross-coupled stiffness, and the slope is direct damping. Fig. 7 shows the fitting curves of the two results. A good linear relationship was observed between tangential force and whirl speed when the CFD model in this study was used. The two curves decreased linearly with whirl speed. The relative error between the two curves decreased with the increase in whirl speed. At whirl speed = 1200 rad/s, the relative error was 2.8 %. The CFD model showed reasonably good agreement with the reference.

3.3 Seal dimensions

Fig. 8 shows the geometry of the two seals. The detailed dimensions are listed in Table 1. The upstream cavity is axially extended to ensure fully developed flow conditions. The radial gap Δ_2 between two lateral teeth is similar to the tip clearance Δ_1 to avoid rubbing between the two lateral teeth.

Table 1. Seal dimensions.

Seal parameters	Value
Number of cavities	8
l_1 (mm)	70
l_2 (mm)	30
l_3 (mm)	5
l_4 (mm)	3
h_1 (mm)	5.5
h_2 (mm)	3.2
w_1 (mm)	0.2
w_2 (mm)	0.2
Δ_1 (mm)	0.5
Δ_2 (mm)	0.5
D (mm)	180
Eccentricity ratio, e	0.2

Table 2. Operating and boundary conditions.

Properties	Value
Preswirl ratio u	10 %–100 %
Outlet pressure P_n (MPa)	1.8
Rotor rotating speed ω (rpm)	6000
Inlet total temperature T_0 (K)	300
Pressure ratio P_r	3–6
Wall	Adiabatic, no slip

3.4 Operating and boundary conditions

The detailed operating and boundary conditions are listed in Table 2.

Fig. 9 shows the computational domain of the two seals. The walls of the stator and rotor were assumed to be adiabatic and nonslip. Faces A and B were set as the pressure inlet and pressure outlet, respectively. Total pressure and total temperature were defined at the inlet boundary, and static pressure was defined at the outlet boundary. These common boundary condition types are widely used for seal models [2, 10, 16, 18].

Face C was set as the FAN boundary to provide preswirl velocity for the working fluid because the working fluid has high-speed circumferential flow before entering the seal. Fig. 10 shows the circumferential flow velocity vectors for seals with and without the FAN boundary. Only the fluid near the rotating wall had a circumferential flow without the FAN boundary. However, all fluids exhibited circumferential flow with the FAN boundary. The flow field was reasonable when the FAN boundary was used.

3.5 Grid independence test

Simulation accuracy depends largely on grid quality. The grid was refined on the meridional plane and circumferential direction independently [18]. Numerous nodes were placed

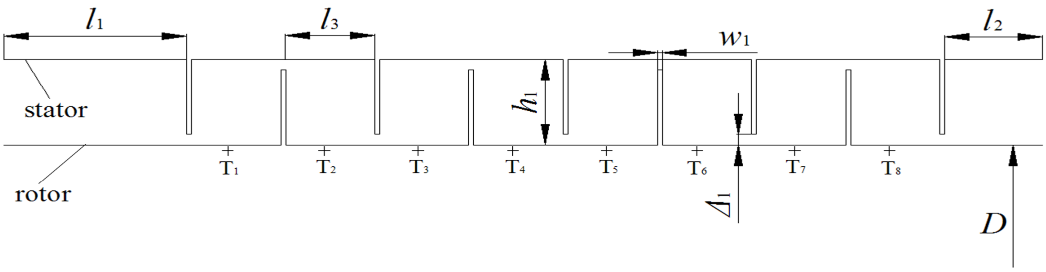

(a) SLS

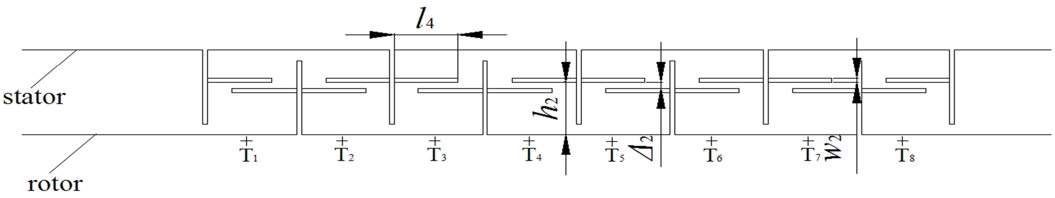

(b) MLS

Fig. 8. Schematic of the seal geometry.

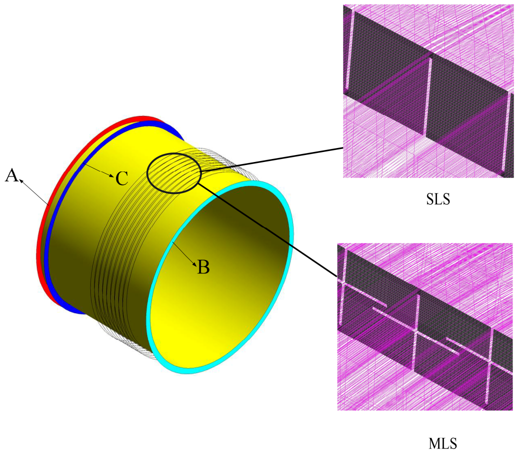

Fig. 9. Computational domain.

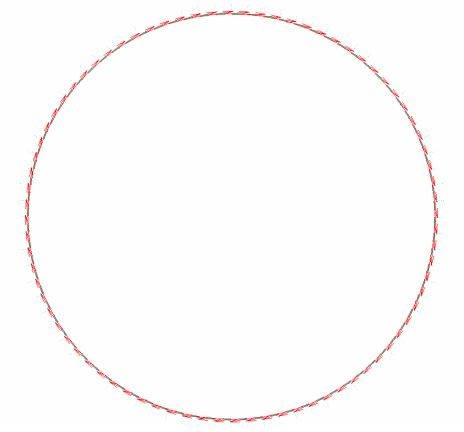

(a) Without FAN boundary

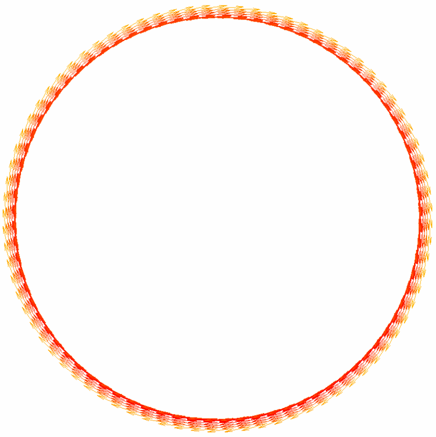

(b) With FAN boundary

Fig. 10. Circumferential flow velocity vectors.

near the rotor and the regions with a small size, considering that the flow fields are considerably complicated and change dramatically. A grid independence test was performed with a seal inlet total pressure of 7.2 MPa, outlet static pressure of 1.8 MPa, and inlet preswirl ratio of 50 %. As shown in Figs. 11 and 12, the test included incremental adjustments to grid size until the leakage and tangential force results were independent. Fig. 13 shows the mesh of the meridional plane after the test. The teeth tip and gap regions were divided into six-layer nodes. The total grid number for SLS and MLS were approximately 876320 and 818720, respectively. In the grid independence test, the values of $y+$ for SLS and MLS were between 34 and 365 and between 37 and 398, respectively, which are acceptable for the wall functions in this study.

Fig. 14 shows the convergence curves of the two seals. Different trial residual values, including the software's default value of 1e-3, were used during the analysis to establish the residual level for convergence. For all seals, the parameters were generally found to converge at a residual value lying between 1e-3 and 1e-6 after 1000 iterations.

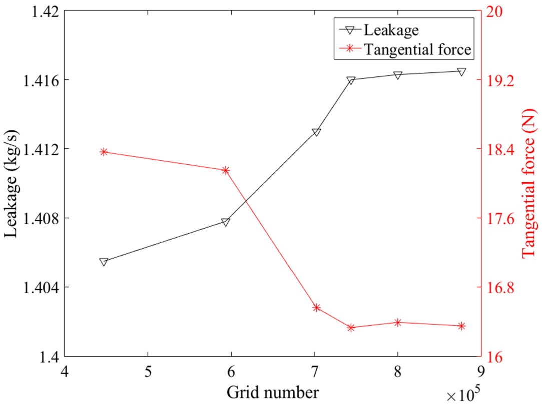

Fig. 11. Influence of grid number on SLS.

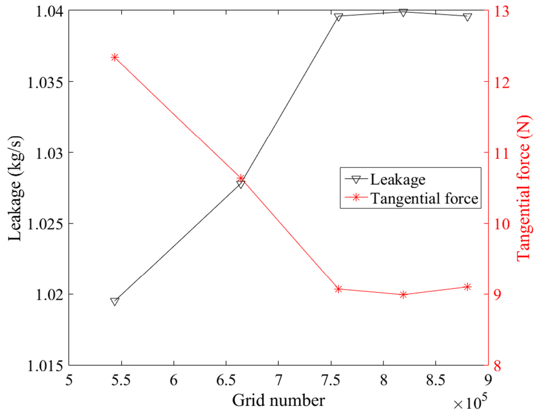

Fig. 12. Influence of grid number on MLS.

4. Fluid structure interface analysis

The computational results showed that the leakage and tangential force of MLS were less than those of SLS. MLS exhibited better seal performance than SLS. However, the external loads acting on the seal teeth may cause deformation of the face, therefore influencing the flow field. The influence of deformation should be analyzed.

The seal teeth can be considered a cantilever-type support. Their deformation distribution can be calculated by the pressure difference acting on two sides of the seal teeth. Fig. 15 shows the total deformation distribution of seal teeth within a seal cavity under the condition of $P_r = 3$. The maximum seal teeth deformation was 0.051 mm, which is about one-tenth of the teeth tip clearance. Fig. 16 shows the variation in maximum total deformation with the pressure ratio. The maximum teeth deformation increased with the increase in the pressure ratio. The maximum seal teeth deformation was 0.08 mm in the case of $P_r = 6$, which is about 16 % of the teeth tip clearance.

The new flow field with the added maximum teeth deformation in the case of $P_r = 6$ was considered. Table 3 shows a comparison of leakage in MLS with and without seal teeth deformation. The influence of seal teeth deformation on leakage was less than 1 %. Table 4 shows the variation in tangential force with the pressure ratio and deformation for MLS. The maximum influence of seal teeth deformation on tangential force was less than 10 %, thereby indicating minimal influence on the flow field. The deformation of lateral teeth can be ignored in this study.

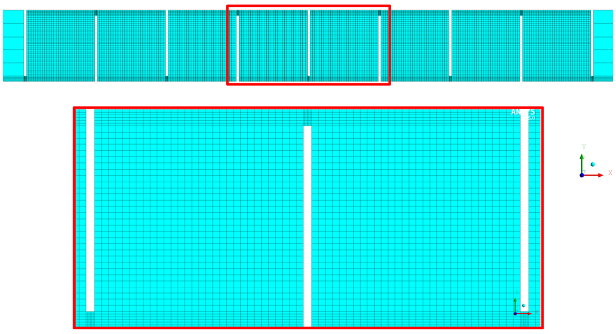

(a) SLS

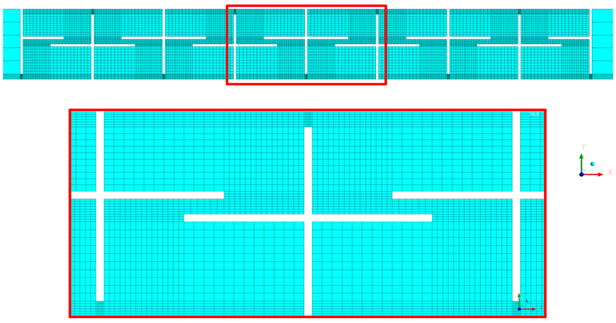

(b) MLS

Fig. 13. Meshes of the meridional plane.

5. Results and discussion

5.1 Flow fields in the two seals

CFD plots were produced to visualize the flow configuration through SLS and MLS. The contours of static pressure are shown in Fig. 17. For SLS, the pressure inside each chamber was almost equal. For MLS, the pressures in the upper and bottom zones of the cavity differed, which indicated that additional throttling existed in the gap between the two lateral teeth. The pressure drop mainly occurred at small orifices because of local resistance. In the seal cavity, the kinetic energy of the fluid dissipated with the vortex and was transformed into thermal energy. Thus, pressure in the seal cavity was almost equal.

The pressures at the seal teeth clearance were used to assess the pressure distribution. For the two seals, the pressures at the vertical teeth clearance were selected because vertical teeth are a common structural feature. The influence of lateral teeth on pressure distribution was then obtained. Fig. 18 shows the pressures at the vertical teeth clearance of the two seals. The pressures were almost equal for the two seals at the same vertical teeth clearance.

Table 3. Variation in leakage with pressure ratio and deformation for MLS.

Pressure ratio	Leakage (kg/s)		Error (%)
	Without deformation	With deformation	
3.0	0.7625	0.7613	0.158
3.5	0.9025	0.9016	0.099
4.0	1.0395	1.0392	0.029
4.5	1.1759	1.1742	0.145
5.0	1.3108	1.3095	0.099
5.5	1.4449	1.4433	0.111
6.0	1.5787	1.5763	0.152

Table 4. Variation in tangential force with pressure ratio and deformation for MLS.

Pressure ratio	Tangential force (N)		Error (%)
	Without deformation	With deformation	
3.0	32.50	33.60	3.4
3.5	38.00	40.78	7.3
4.0	45.00	46.71	3.8
4.5	50.00	51.57	3.1
5.0	57.12	58.07	1.7
5.5	64.83	65.55	1.1
6.0	77.00	78.00	1.3

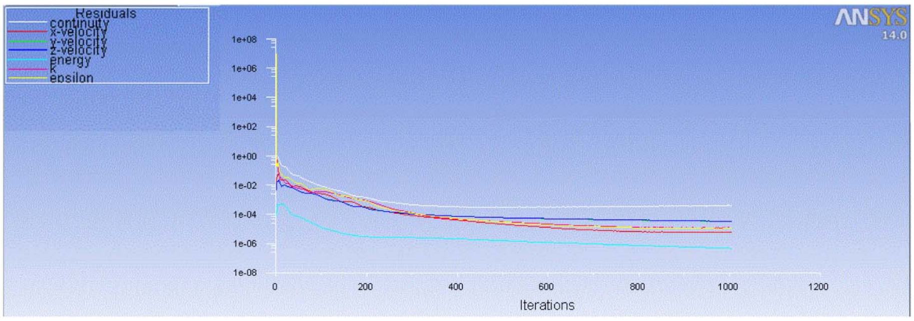

(a) Residual convergence curve for SLS

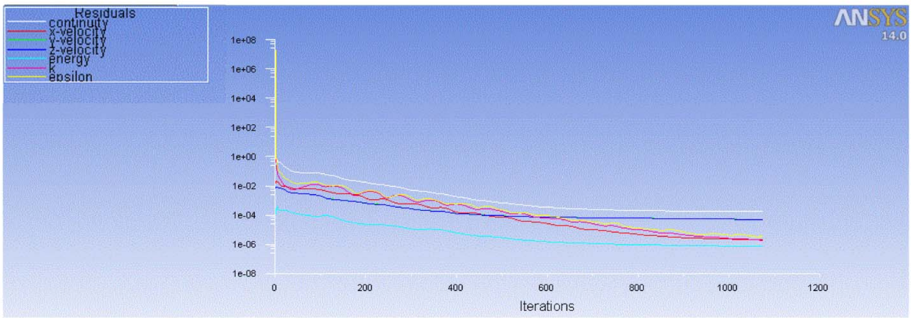

(b) Residual convergence curve for MLS

Fig. 14. Residual curves of the computational process.

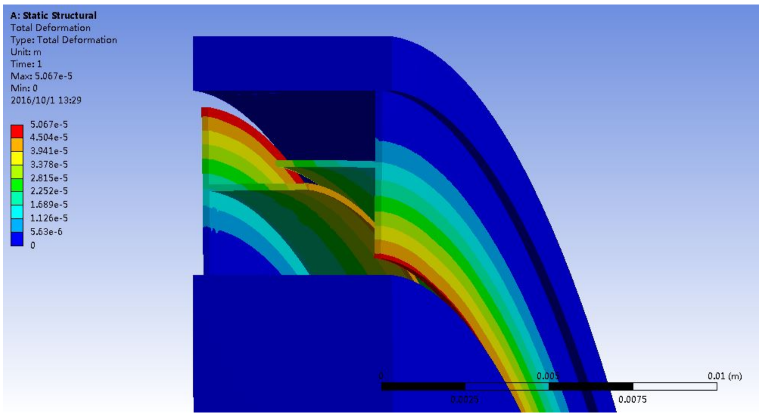

Fig. 15. Deformation distribution of seal teeth.

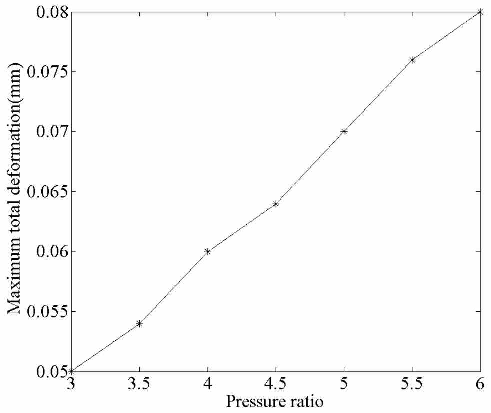

Fig. 16. Variation in maximum total deformation with pressure ratio (u = 100 %, ω = 6000 rpm).

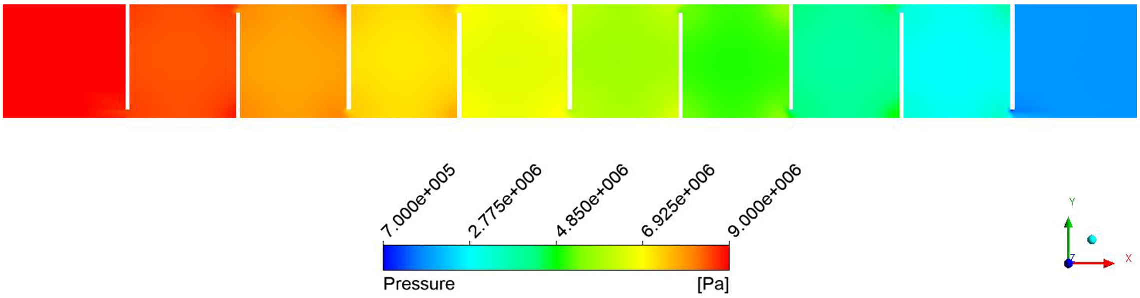

(a) SLS

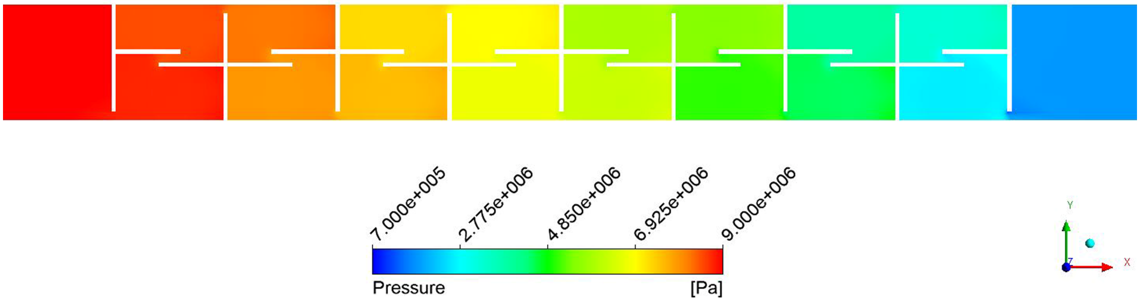

(b) MLS

Fig. 17. Contours of static pressure.

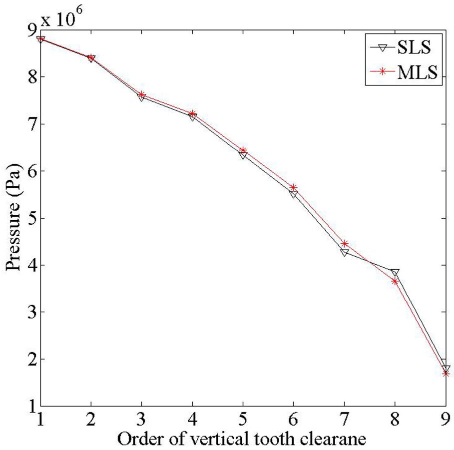

Fig. 18. Pressure at the vertical teeth clearance of the two seals.

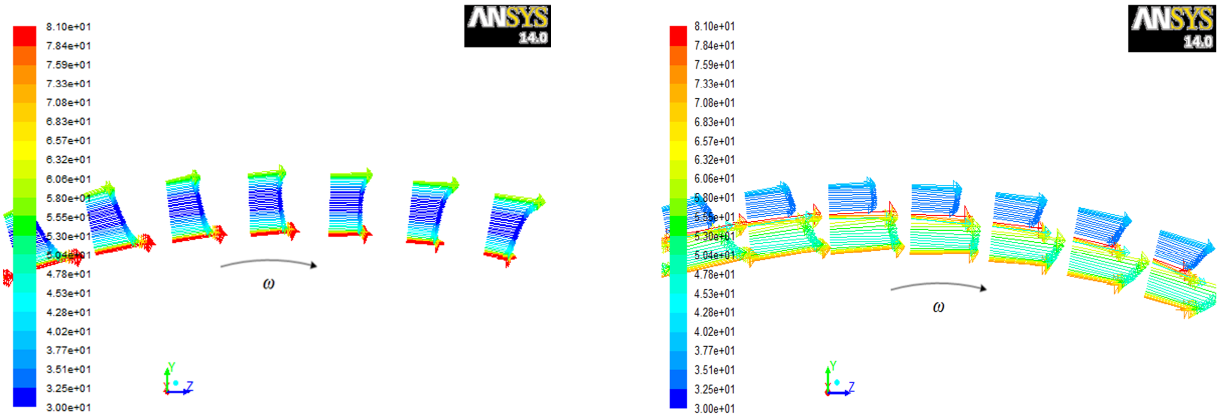

(a) SLS (b) MLS

Fig. 19. Flow fields on the perpendicular plane of the flow direction for the two seals.

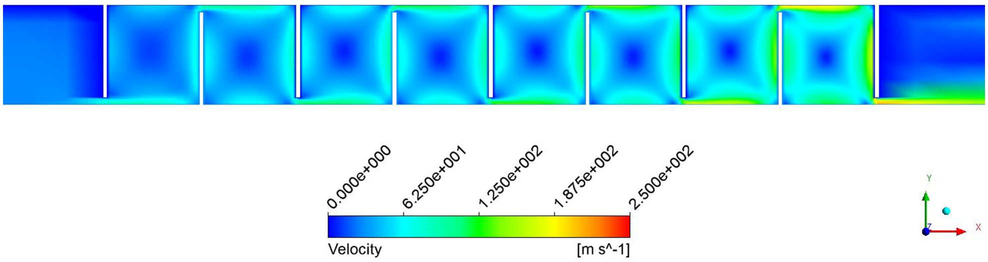

(a) SLS

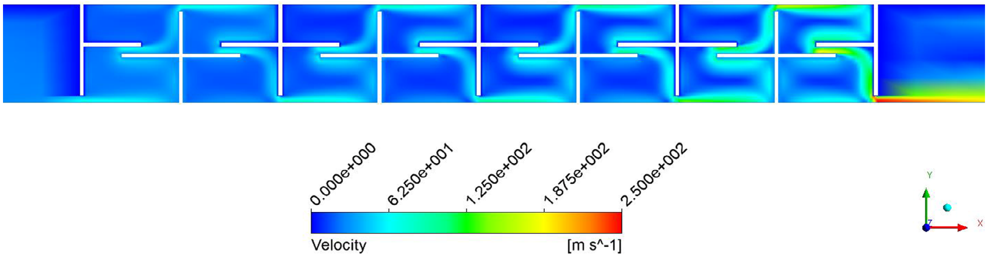

(b) MLS

Fig. 20. Contours of velocity.

Fig. 19 shows the flow fields on the perpendicular plane of the flow direction in the first cavity in the two seals. In the flow channel, the working fluid was affected by the rotating face and exhibited tangential momentum because of the viscosity effect. Thus, the tangential flow direction was similar to the rotating direction. Fig. 20 shows the velocity contours of the two seals. Velocity increased according to the mass conservation law because the flow area suddenly contracted at the small clearance.

Fig. 21 shows the velocity vectors in the seal cavity. A high-speed jet at small orifices and a large vortex inside each chamber were observed because of the viscous force between jet and cavity flows. Kinetic energy dissipated with the vortex, and a certain portion of flow was directly carried over to the next tooth without being dissipated in the cavity. Compared with SLS, which has only one recirculation zone, MLS had a twin vortex pattern in its cavity. At the same time, the high-speed jet was deflected by 90° when the jet flowed through orifices in the seal teeth tip. An additional 180° deflection occurred in the gap between two lateral teeth within MLS, resulting in increased flow separation and flow disturbance for MLS.

5.2 Leakage analysis

Fig. 22 shows the leakage comparison between SLS and MLS. The leakage increased with the increase in pressure ratio. The leakage of MLS was about 30 % lower than that of SLS.

Turbulent kinetic energy k_t and turbulent viscosity μ_t can be used to evaluate the effectiveness of leakage control. They are defined as

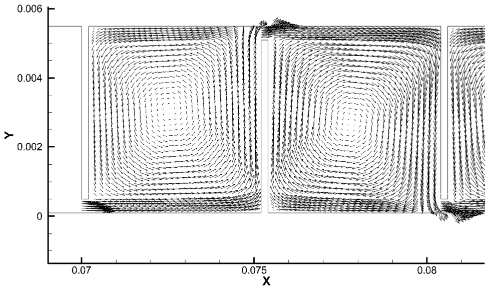

(a) SLS

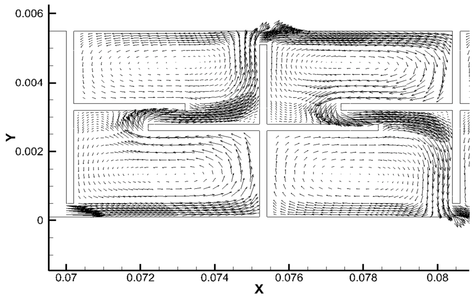

(b) MLS

Fig. 21. Velocity vectors.

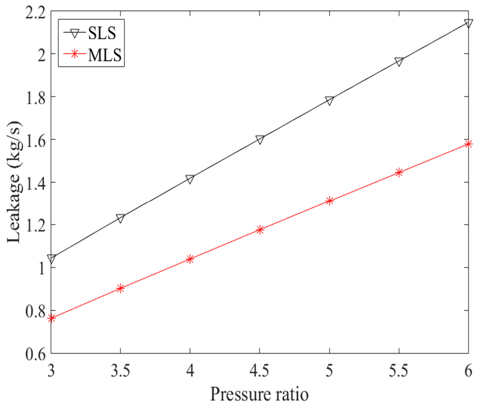

Fig. 22. Variation in leakage with pressure ratio (u = 100 %, ω = 6000 rpm).

$$k_t = 1.5 * (v * I)^2 , \tag{8}$$

$$\mu_t = \rho C_\mu k_t^2 / \varepsilon_t , \tag{9}$$

where v is the average velocity, I is the turbulent intensity, ρ is the density of fluid, C_μ is the empirical coefficient, and ε_t is the turbulence eddy dissipation.

Fig. 23 shows the contours of the turbulent kinetic energy of the two seals. The maximum turbulent kinetic energy value occurred near the stagnation region where the flow decelerated. For SLS, the maximum turbulent kinetic energy value occurred at the teeth tip. However, for MLS, given the existence of lateral teeth, the maximum turbulent kinetic energy values occurred at the seal teeth tip and the gap between the two lateral teeth. Notably, the region of MLS with high turbulent kinetic energy was larger than that of SLS. Hence, dissipation of the main flow momentum through turbulent kinetic energy production was higher for MLS.

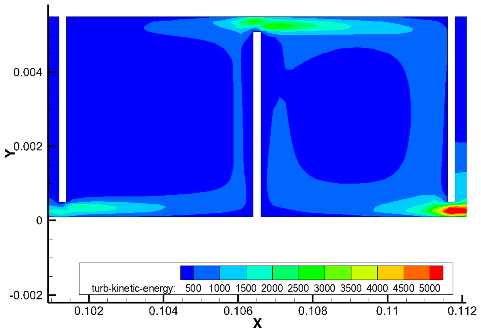

(a) SLS

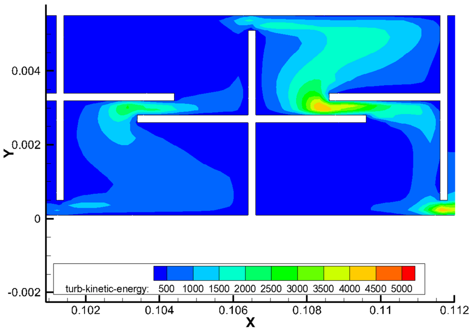

(b) MLS

Fig. 23. Contours of turbulent kinetic energy of the two seals.

The contours of the turbulent viscosity of the two seals are shown in Fig. 24. The maximum turbulent viscosity values of the seal cavity within SLS and MLS were approximately 0.14 and 0.24 kg/(m·s), respectively. The average turbulent viscosity of MLS was higher than that of SLS. This finding indicates that the leakage flow within MLS suffered from more flow resistance. Given that MLS has higher turbulent kinetic energy and turbulent viscosity, the leakage of MLS was less than that of SLS.

The leakage flow paths of the two seals are plotted in Fig. 25. Notably, a longer and more complicated leakage path occurred in MLS compared with SLS. This finding indicates more flow separation, flow disturbance, and vena contracta effect for MLS, which are helpful in leakage control.

5.3 Cross-coupled stiffness analysis

The nonuniform pressure distribution in the seal cavity generates a seal force that acts on the rotor, which can be divided into radial force and tangential force, as shown in Figs. 26 and 27. Tangential force, which is orthogonal to the direction of eccentricity, is considered the major cause of rotor instability. Fig. 28 shows the variation in tangential force with the pressure ratio. The tangential force of MLS was less than that of SLS. Fig. 29 shows that the tangential force of MLS gradually

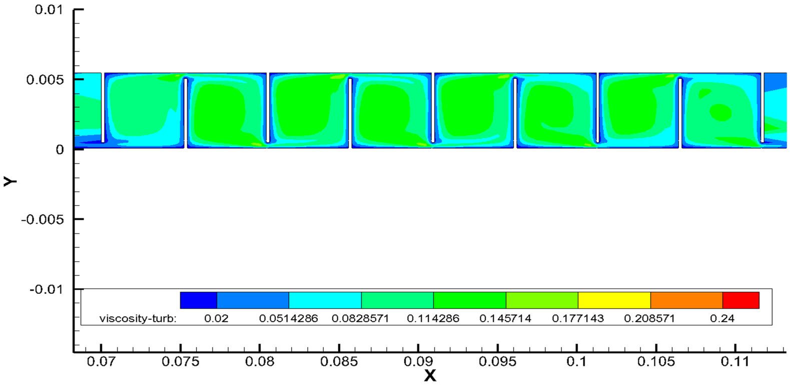

(a) SLS

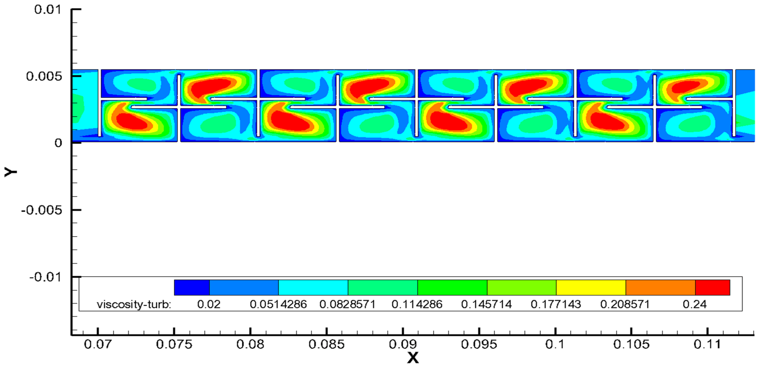

(b) MLS

Fig. 24. Contours of the turbulent viscosity of the two seals.

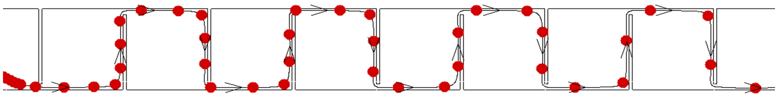

(a) SLS

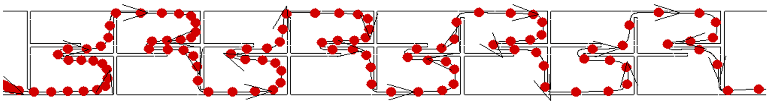

(b) MLS

Fig. 25. Leakage path of the two seals.

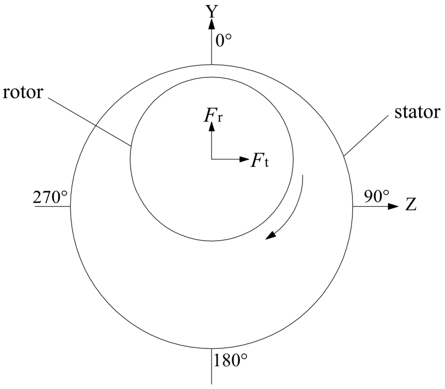

Fig. 26. Seal force model of the perpendicular plane of the flow direction.

increased with the preswirl ratio. In high-speed rotating machinery, the inlet preswirl velocity is high. MLS has a smaller tangential force with high preswirl ratio compared with SLS.

By disregarding add-mass coefficients and assuming a circular whirl orbit around the seal center, the reaction force model can be reduced to the following expression [19].

$$\begin{Bmatrix} F_z \\ F_y \end{Bmatrix} = -\begin{pmatrix} K & k \\ -k & K \end{pmatrix}\begin{Bmatrix} z \\ y \end{Bmatrix} - \begin{pmatrix} C & c \\ -c & C \end{pmatrix}\begin{Bmatrix} \dot{z} \\ \dot{y} \end{Bmatrix}, \tag{10}$$

where F_z and F_y are the components of reaction forces acting on the rotor, z and y define the components of the seal–rotor displacements relative to the stator, and rotordynamic coefficients K, k, C and c are the direct stiffness, cross-coupled stiff-

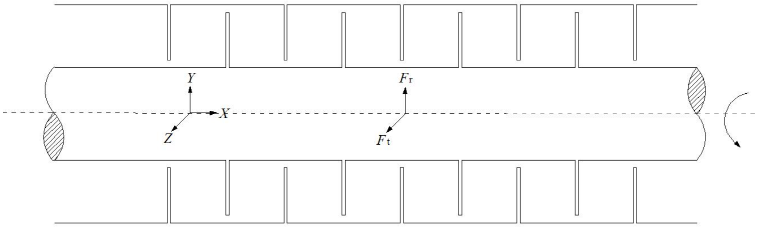

(a) SLS

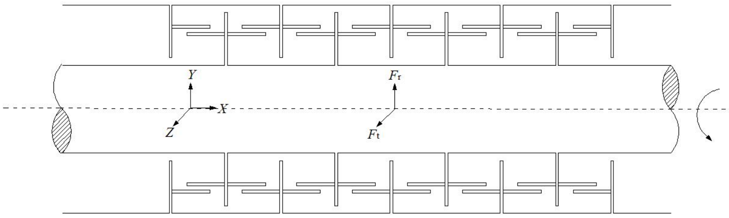

(b) MLS

Fig. 27. Seal force model of the cross profile along the rotor axis.

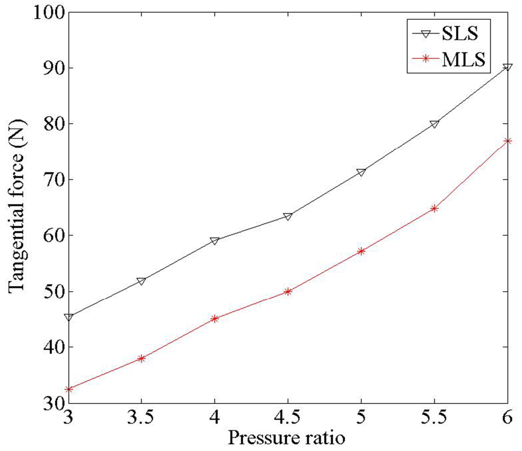

Fig. 28. Variation in tangential force with pressure ratio (u = 100 %, ω = 6000 rpm).

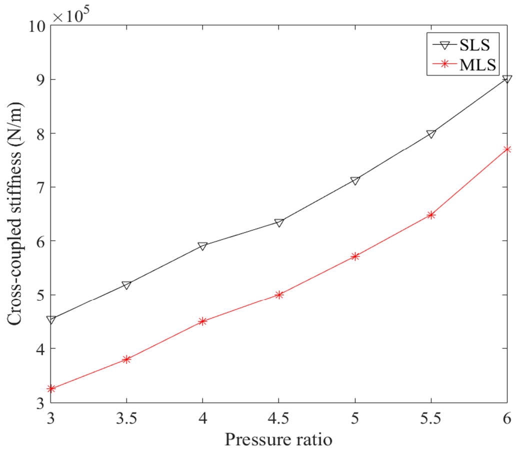

Fig. 30. Variation in cross-coupled stiffness with pressure ratio (u = 100 %, ω = 6000 rpm).

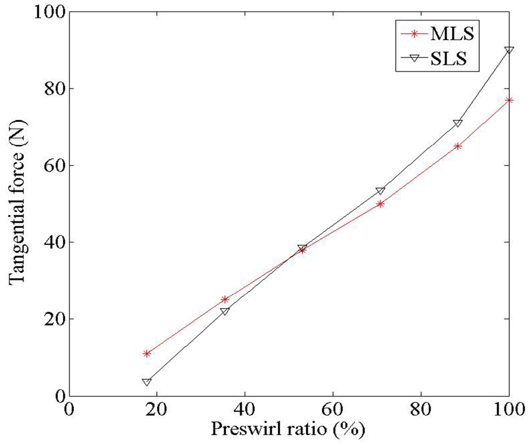

Fig. 29. Variation in tangential force with preswirl ratio (P_r = 6, ω = 6000 rpm).

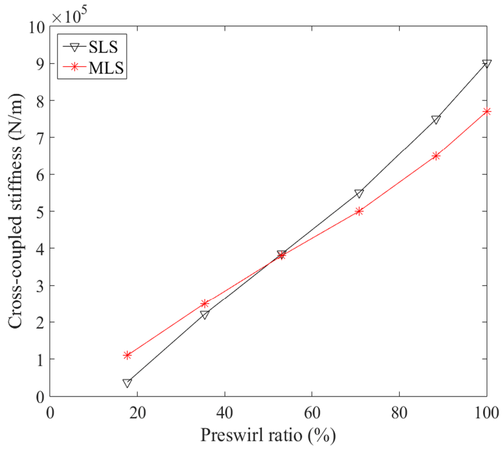

Fig. 31. Variation in cross-coupled stiffness with preswirl ratio (P_r = 6, ω = 6000 rpm).

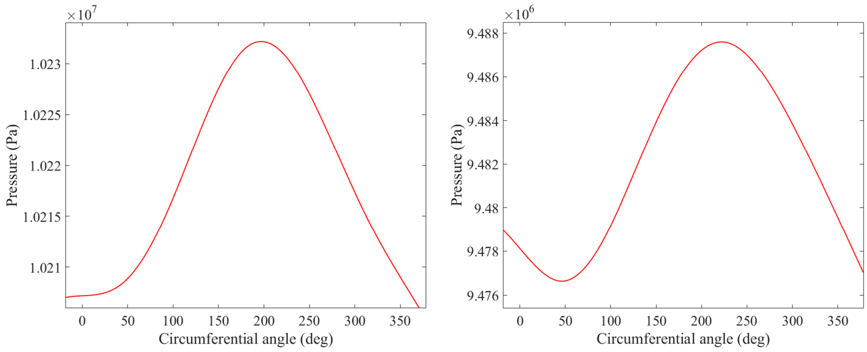

T_1 section T_2 section

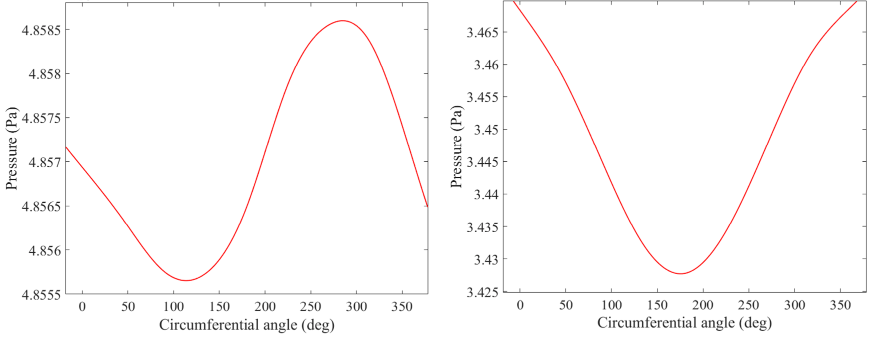

T_7 section T_8 section

(a) SLS

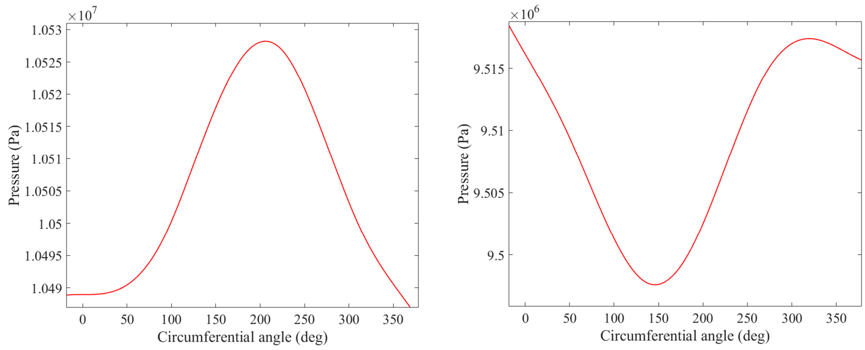

T_1 section T_2 section

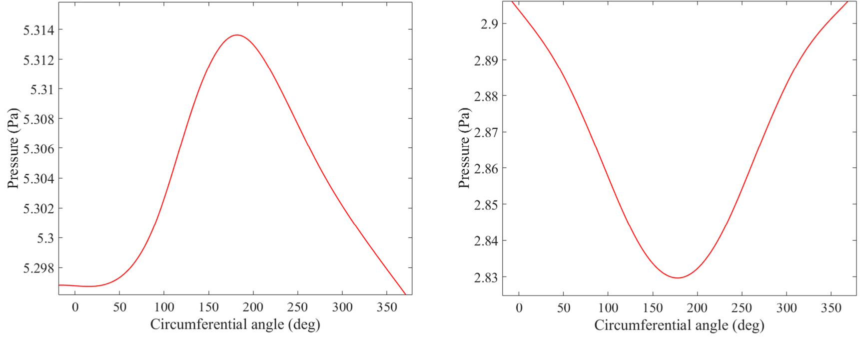

T_7 section T_8 section

(b) MLS

Fig. 32. Circumferential pressure distribution.

ness, direct damping, and cross-coupled damping, respectively.

Cross-coupled stiffness *k* can cause rotordynamic instability in turbomachinery. Cross-coupled stiffness should have a low or negative value to keep the seal system stable [14]. Fig. 30 shows the change in cross-coupled stiffness with the pressure ratio. The cross-coupled stiffness of MLS was about 75 % to 85 % that of SLS. Fig. 31 shows the change in cross-coupled stiffness with the preswirl ratio. The cross-coupled stiffness of MLS gradually increased with the preswirl ratio and was less sensitive to inlet preswirl velocity. The difference in cross-coupled stiffness between the two seals increased at a high preswirl ratio.

Cross-coupled stiffness is governed by tangential force [19], which originates from the nonuniform pressure distribution in the seal cavity [20]. Fig. 32 shows the circumferential pressure distribution near the rotor surface (see Fig. 8) in the first two seal cavities (T_1 and T_2) and the last two seal cavities (T_7 and T_8). For SLS, the highest and lowest pressure spots of the T_1 section were located at the angle with the largest and smallest clearances (see Fig. 26), respectively. From the T_1 section to the T_8 section, the highest and lowest pressure spots moved along the rotating direction gradually. Notably, the highest pressure spot angle difference between T_1 and T_8 sections was about 180°. The movement of the high-pressure spot toward the rotating direction demonstrated the existence of axial spiral flow in SLS, which was the main cause of fluid-induced force. For MLS, the highest pressure spot was at the angle with the largest clearance in the T_1 section, similar to that in SLS. However, in the T_2 section, the highest pressure spot was at the angle with the smallest clearance. From the T_1 section to the T_2 section, the angle of the highest pressure spot changed by 180° dramatically. The next two cavities (T_3 and T_4) followed the same pressure distribution law as the first two cavities (T_1 and T_2). From the T_1 section to the T_8 section, the angles of the highest and lowest pressure spots changed by 180° alternatively. In each cavity, the largest and smallest pressure spots were located at the largest and smallest clearances, respectively, or at the smallest and largest clearances, respectively. The destabilizing tangential force was averaged to a small value.

6. Structural parameter analysis

The height and gap of lateral teeth are two major parameters that affect the performance of MLS. These factors should be investigated.

6.1 Lateral teeth height

Relative height γ was defined to describe the radial position of the lateral teeth in the seal cavity.

$$\gamma = h_2 / h_1 . \tag{11}$$

Table 5 and Fig. 33 show the variation in the leakage and cross-coupled stiffness with γ, respectively. The influence of γ on leakage was less than 4 %. However, cross-coupled stiffness was sensitive to γ. Thus, cross-coupled stiffness was optimized to set the lateral teeth in the middle position of the seal cavity.

Table 5. Variation in leakage with lateral teeth height.

γ	Leakage (kg/s)	Error (%)
0.22	1.617	/
0.27	1.602	0.93
0.31	1.585	1.98
0.36	1.553	3.96
0.42	1.567	3.09
0.47	1.573	2.72
0.53	1.581	2.23
0.58	1.578	2.41
0.64	1.579	2.35
0.73	1.609	0.01

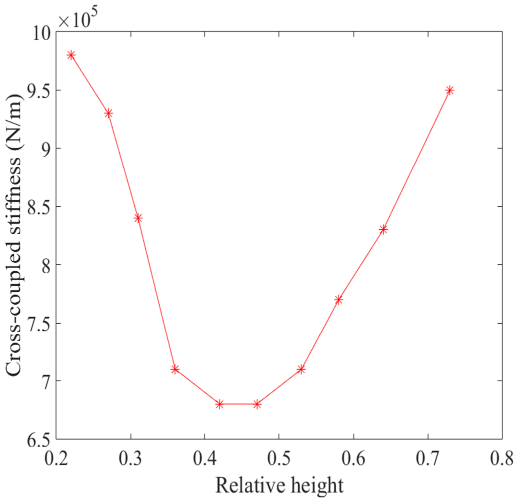

Fig. 33. Variation in cross-coupled stiffness with lateral teeth height.

6.2 Lateral teeth gap

Fig. 34 shows that the leakage increases with lateral teeth gap Δ_2. Labyrinth seals are non-contact seals, in which sealing is performed by a series of throttles and cavities. Physically, the pressure difference between the inlet and outlet is the driving force, and throttle provides local resistance for the flow in the seal. The large area of the throttle results in small local resistance. Thus, increased lateral teeth gap Δ_2 results in small flow resistance and large leakage.

From another point of view, Li [21] derived a simple equation to express the relation between leakage *M* and seal tooth gap Δ for the labyrinth seal.

$$M = C_m \sqrt{\Delta^3} \sqrt{P_o^2 - P_n^2} , \tag{12}$$

Table 6. Variation in cross-coupled stiffness with lateral teeth gap.

Δ_2 (mm)	Cross-coupled stiffness (N/m)	Error (%)
0.5	770000	/
0.6	780000	1.30
0.7	790000	2.60
0.8	780000	1.30
0.9	790000	2.60
1.0	790000	2.60
1.1	790000	2.60
1.2	800000	3.90

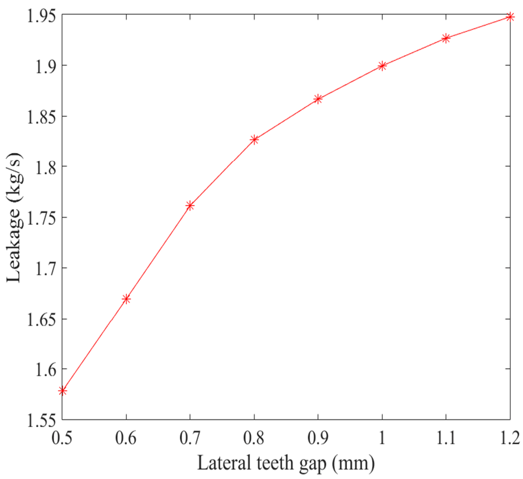

Fig. 34. Variation in leakage with lateral teeth gap.

where M is the leakage, Δ is the tooth gap, P_0 is the inlet pressure, P_n is the outlet pressure, and C_m is the empirical coefficient.

Numerically, the leakage increases with the increase in teeth gap because $\left(\partial M/\partial \Delta\right)$ is positive.

Table 6 shows the variation in cross-coupled stiffness with lateral teeth gap Δ_2. Cross-coupled stiffness was insensitive to Δ_2, and the error was less than 4 %. Lateral teeth gap Δ_2 should be set similar to tip clearance Δ_1 to avoid rubbing between the two lateral teeth.

7. Conclusions

MLS with specially designed lateral teeth on SLS was proposed. The lateral teeth changed the flow field within the labyrinth seal. Through an in-depth CFD analysis, several conclusions were obtained as follows:

(1) The turbulent dissipation effect in MLS was stronger than that in SLS, and the leakage flow encountered more resistance. The leakage in MLS was about 30 % lower than that in SLS.

(2) The cross-coupled stiffness of MLS was about 75 % to 85 % that of SLS, and the cross-coupled stiffness of MLS was less sensitive to the preswirl ratio. MLS performed better in suppressing rotor vibration, particularly in the case with a high preswirl ratio.

(3) The lateral teeth should be set in the middle of the seal cavity, and the gap of the lateral teeth should be set similar to the tip clearance to optimize the performance of MLS.

Acknowledgment

This study was supported by the National Natural Science Foundation of China (Nos. 51575105 and 51275088).

Nomenclature

A : Teeth tip clearance flow area (m^2)
B : Lateral teeth gap flow area (m^2)
C_μ : Empirical coefficient
D : Diameter of the rotor (mm)
e : Eccentricity ratio
F_r : Radial seal force (N)
F_t : Tangential seal force (N)
h_1 : Seal cavity height (mm)
h_2 : Lateral teeth height (mm)
I : Turbulent intensity
k_t : Turbulence kinetic energy (m^2/s^2)
l_1 : Upstream cavity length (mm)
l_2 : Downstream cavity length (mm)
l_3 : Seal cavity length (mm)
l_4 : Lateral tooth length (mm)
M : Mass flow rate (kg/s)
M_{MLS} : Mass flow rate of the MLS (kg/s)
M_{SLS} : Mass flow rate of the SLS (kg/s)
n : Number of seal teeth
P_r : Pressure ratio
P_0 : Inlet pressure (Pa)
P_n : Outlet pressure (Pa)
R_g : Gas constant (J/kg·K)
T_0 : Inlet total temperature (K)
u : Inlet preswirl ratio
v : Average velocity (m/s)
w_1 : Vertical tooth width (mm)
w_2 : Lateral tooth width (mm)
ω : Rotating speed (rpm)
Ω : Whirl speed (rpm)
ρ : Density of fluid (kg/m^3)
ε_t : Turbulence eddy dissipation (m^2/s^3)
μ_t : Turbulent viscosity (kg/m·s)
β : Function of P_0/P_n
γ : Relative height
δ : Eccentricity
Δ_1 : Tooth tip clearance (mm)
Δ_2 : Lateral teeth gap (mm)
CFD : Computational fluid dynamics
MLS : Mixed labyrinth seal
SFC : Specific fuel consumption
SLS : Staggered labyrinth seal

References

[1] H. L. Stocker, Advanced labyrinth seal design performance for high pressure ratio gas turbines, *ASME 1975 Winter Annual Meeting*, Houston, Texas, USA, 30 November - 5 December 1975, paper no. 75-WA/GT-22, pp. V001T01A005. New York: ASME.

[2] R. Gao and G. Kirk, CFD study on stepped and drum balance labyrinth seal, *Tribol. Trans.*, 56 (4) (2013) 663-671.

[3] R. Gao, Computational fluid dynamic and rotordynamic study on the labyrinth seals, *Ph.D. Thesis*, Virginia Polytechnic Institute and State University, USA (2012).

[4] W. Z. Wang et al., Numerical analysis of leakage flow through two labyrinth seals, *J. Hydrodyn, Ser. B*, 19 (1) (2007) 107-112.

[5] D. L. Rhode, J. W. Johnson and D. H. Broussard, Flow visualization and leakage measurements of stepped labyrinth seals: part 1—annular groove, *J. Turbomach*, 119 (4) (1997) 839-843.

[6] D. L. Rhode, S. H. Ko and G. L. Morrison, Experimental and numerical assessment of an advanced labyrinth seal, *Tribol. Trans.*, 37 (4) (1994) 743-750.

[7] S. P. Asok et al., Neural network and CFD-based optimisation of square cavity and curved cavity static labyrinth seals, *Tribol. Int.*, 40 (7) (2007) 1204-1216.

[8] J. M. Vance and J. M. Li, Test results of a new damper seal for vibration reduction in turbomachinery, *J. Eng. Gas Turbines Power*, 118 (4) (1996) 843-846.

[9] A. M. G. Eldin, Leakage and rotordynamic effects of pocket damper seals and see-through labyrinth seals, *Ph.D. Thesis*, Texas A&M University, USA (2007).

[10] G. Kirk and R. Gao, Influence of preswirl on rotordynamic characteristics of labyrinth seals, *Tribol. Trans.*, 55 (3) (2012) 357-364.

[11] Z. G. Li, J. Li and Z. P. Feng, Numerical comparison of rotordynamic characteristics for a fully partitioned pocket damper seal and a labyrinth seal with high positive and negative inlet preswirl, *J. Eng. Gas Turbines Power*, 138 (4) (2015) 042505-042505-13.

[12] E. A. Baskharone, Swirl brake effect on the rotordynamic stability of a shrouded impeller, *J. Turbomach.*, 121 (1) (1999) 127-133.

[13] D. W. Childs et al., Rotordynamic performance of a negative-swirl brake for a tooth-on-stator labyrinth seal, *J. Eng. Gas Turbines Power*, 138 (6) (2015) 062505-062505-8.

[14] E. A. Soto and D. W. Childs, Experimental rotordynamic coefficient results for: (a) a labyrinth seal with and without shunt injection and (b) a honeycomb seal, *J. Eng. Gas Turbines Power*, 121 (1) (1999) 153-159.

[15] H. L. Stoker, D. M. Cox and G. F. Holle, Aerodynamic performance of conventional and advanced design labyrinth seals with solid-smooth, abradable and honeycomb lands, *NASA Technical Report*, Report no. NASA-CR-135307, 21 Jul 1976-21 Nov (1977).

[16] Z. G. Li, J. Li and Z. P. Feng, Numerical investigations on the leakage and rotordynamic characteristics of pocket damper seals-part II: effects of partition wall type, partition wall number, and cavity depth, *J. Eng. Gas Turbines Power*, 137 (3) (2014) 032504-032504-13.

[17] W. J. Kearton and T. H. Keh, Leakage of air through labyrinth glands of staggered type, *Proc. IMechE, Part A: J. Power and Energy*, 166 (1952) 180-195.

[18] T. Hirano, Z. L. Guo and R. G. Kirk, Application of computational fluid dynamics analysis for rotating machinery—part II: labyrinth seal analysis, *J. Eng. Gas Turbines Power*, 127 (4) (2005) 820-826.

[19] A. O. Pugachev, U. Kleinhans and M. Gaszner, Prediction of rotordynamic coefficients for short labyrinth gas seals using computational fluid dynamics, *J. Eng. Gas Turbines Power*, 134 (6) (2012) 062501-062501-10.

[20] S. H. Kim and T. W. Ha, Prediction of leakage and rotordynamic coefficients for the circumferential-groove-pumb seal using CFD analysis, *Journal of Mechanical Science and Technology*, 30 (5) (2016) 2037-2043.

[21] Z. R. Li et al., Investigation and improvement of the staggered labyrinth seal, *Chin. J. Mech. Eng-En.*, 28 (2) (2015) 402-408.

[22] S. Subramanian, A. S. Sekhar and B. V. S. S. S. Prasad, Influence of combined radial location and growth on the leakage performance of a rotating labyrinth gas turbine seal, *Journal of Mechanical Science and Technology*, 29 (6) (2015) 2535-2545.

Mingjie Zhang is studying for his Master's degree in engineering science in the Department of Power Engineering, Southeast University. His research interests include rotordynamics and flow-induced vibration in turbomachinery.

Jiangang Yang received his Ph.D. from the Department of Power Engineering, Southeast University, in 1995 and is the Deputy Director of National Engineering Research Center of Turbo-generator Vibration. His research areas include rotating machinery fault monitoring and diagnosis, rotordynamics, and flow-induced vibration.